

PAPER • OPEN ACCESS

Machine learning-based signal quality assessment for cardiac volume monitoring in electrical impedance tomography

To cite this article: Chang Min Hyun *et al* 2023 *Mach. Learn.: Sci. Technol.* **4** 015034

View the [article online](#) for updates and enhancements.

You may also like

- [Time-dependent dielectric breakdown of MgO magnetic tunnel junctions and novel test method](#)
Kyungjun Kim, Chulmin Choi, Youngtaek Oh *et al.*
- [Cyclic Voltammetry Stripping Analysis to Determine Iodide Ion Concentration in Cu Plating Bath](#)
Young Yoon, Yu Seok Ham, Tae Young Kim *et al.*
- [Linear nonsaturating magnetoresistance in kagome superconductor CsV₃Sb₆ thin flakes](#)
Xinjian Wei, Congkuan Tian, Hang Cui *et al.*



PAPER

OPEN ACCESS

RECEIVED
3 January 2023REVISED
3 March 2023ACCEPTED FOR PUBLICATION
21 March 2023PUBLISHED
30 March 2023

Original Content from
this work may be used
under the terms of the
[Creative Commons
Attribution 4.0 licence](#).

Any further distribution
of this work must
maintain attribution to
the author(s) and the title
of the work, journal
citation and DOI.



Machine learning-based signal quality assessment for cardiac volume monitoring in electrical impedance tomography

Chang Min Hyun¹ , Tae Jun Jang¹, Jeongchan Nam², Hyeuknam Kwon³, Kiwan Jeon⁴
and Kyounghun Lee^{5,*}

¹ School of Mathematics and Computing (Computational Science and Engineering), Yonsei University, Seoul, Republic of Korea

² BiLab, Seongnam, Republic of Korea

³ Division of Software, Yonsei University, Wonju, Republic of Korea

⁴ National Institute for Mathematical Sciences, Daejeon, Republic of Korea

⁵ Kyung Hee University, Seoul, Republic of Korea

* Author to whom any correspondence should be addressed.

E-mail: imlk84@gmail.com

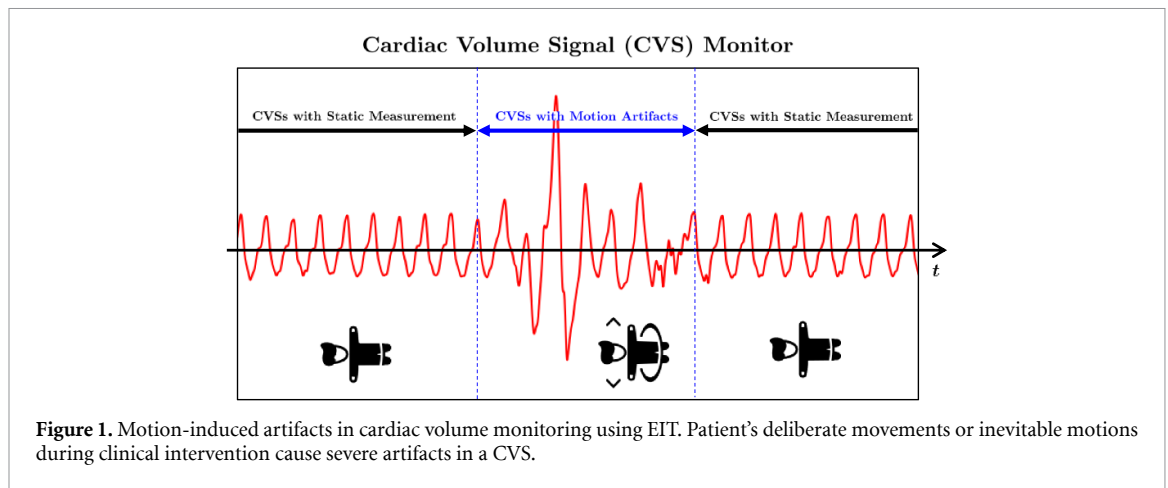
Keywords: cardiac volume monitoring, electrical impedance tomography, machine learning, signal quality assessment

Abstract

Owing to recent advances in thoracic electrical impedance tomography (EIT), a patient's hemodynamic function can be noninvasively and continuously estimated in real-time by surveilling a cardiac volume signal (CVS) associated with stroke volume and cardiac output. In clinical applications, however, a CVS is often of low quality, mainly because of the patient's deliberate movements or inevitable motions during clinical interventions. This study aims to develop a signal quality indexing method that assesses the influence of motion artifacts on transient CVSs. The assessment is performed on each cardiac cycle to take advantage of the periodicity and regularity in cardiac volume changes. Time intervals are identified using the synchronized electrocardiography system. We apply divergent machine-learning methods, which can be sorted into discriminative-model and manifold-learning approaches. The use of machine-learning could be suitable for our real-time monitoring application that requires fast inference and automation as well as high accuracy. In the clinical environment, the proposed method can be utilized to provide immediate warnings so that clinicians can minimize confusion regarding patients' conditions, reduce clinical resource utilization, and improve the confidence level of the monitoring system. Numerous experiments using actual EIT data validate the capability of CVSs degraded by motion artifacts to be accurately and automatically assessed in real-time by machine learning. The best model achieved an accuracy of 0.95, positive and negative predictive values of 0.96 and 0.86, sensitivity of 0.98, specificity of 0.77, and AUC of 0.96.

1. Introduction

Over several decades, continued advances in electrical impedance tomography (EIT) have expanded the clinical capability of real-time cardiopulmonary monitoring systems by overcoming the limitations of traditional methods, such as cardiac catheterization through blood vessels [4, 9, 18, 19, 29, 30, 39, 43, 60]. Recently, based on thoracic EIT, a patient's hemodynamic function can be noninvasively and continuously estimated in real-time by surveilling a signal extracted using EIT, the so-called cardiac volume signal (CVS), which has a strong relationship with key hemodynamic factors such as stroke volume and cardiac output [5, 28, 54]. In clinical applications, however, a CVS is often of low quality, mainly because of the patient's deliberate movements or inevitable motions during clinical interventions such as medical treatment and nursing. Because postural change causes movement of the chest boundary to which existing EIT solvers are highly sensitive owing to time-difference-reconstruction characteristics [1, 8, 33, 38, 47], motion-induced artifacts are generated in the CVS, as shown in figure 1.



CVS extraction is to separate a cardiogenic component from the EIT voltage data, resulting from current injections at electrodes attached across a human chest. Since the development of impedance cardiography more than 40 years ago [29], there have been numerous efforts for the accurate and reliable separation of weak cardiogenic component toward the clinical use. In the studies [18, 30, 60], effective techniques were developed, but they need the hypertonic saline injection as a contrast agent [9], which may decrease the clinical capability in terms of non-invasive and long-term continuous monitoring. Recently, Jang *et al* [28] developed a contrast agent injection-free separation method that is based on spatial filtering using the statistical independence assumption of the cardiogenic impedance change to other changes. However, its practical performance may be restricted due to the strong assumption. Lee *et al* [41] then suggested a new spatial-filtering method that instead takes advantage of timing constraints from electrocardiography (ECG) and validated its effectiveness from *in vivo* animal data. Thanks to these endeavors, effective and fully non-invasive CVS extraction is currently capable with motion-free measurements where voltage data are mainly influenced by air and blood volume changes in the lungs, heart, and blood vessels comprehensively, but not by motions. In contrast, achieving the CVS extraction in motion-influenced measurements is still a long-term challenge. Postural changes in EIT measurements cause strong distortion of the voltage data [1, 59] and easily disturb the extraction of relatively weak cardiogenic signals [7, 34, 42].

Handling motion interference has been a huge challenge in most EIT-based techniques for enhancing clinical capability, but not researched much yet [57]. Adler *et al* [1] and Zhang and Patterson [59] investigated the negative motion effect in the EIT. Soleimani *et al* [46] and Dai *et al* [17] proposed a motion-induced artifact reduction method by reconstructing electrode movements along with conductivity changes. Lee *et al* [38] analyzed motion artifacts in EIT measurements and proposed a subspace-based artifact rejection method. Yang *et al* [57] suggested the discrete wavelet transform-based approach that reduces motion artifacts of three specific types. However, clinical motion artifacts are still not effectively addressed because of practical motion's immense diversity and complexity. Accordingly, for the time being, the EIT-based hemodynamic monitoring system attempts to be preferentially developed toward filtering motion-influenced CVSs rather than recovering them. In the clinical environment, this filtration can provide immediate warnings so that clinicians can minimize confusion regarding the patient's condition, reduce clinical resource utilization, and improve the confidence level of the monitoring system [16].

This study aims to develop a signal quality indexing (SQI) method that assesses whether motion artifacts influence transient CVSs. To take advantage of the periodicity and regularity in cardiac volume changes, the assessment is performed on each cardiac cycle, whose time intervals are identified using the synchronized ECG system. We leverage machine learning (ML), which has provided effective solutions for various biosignal-related tasks through feature disentanglement of complicated signals [6, 10, 14, 26, 36, 50, 51, 55]. The use of ML could be suitable for our real-time monitoring application that requires fast inference and automation as well as high accuracy.

We apply divergent ML methods, which can be sorted into discriminative-model and manifold-learning approaches. The discriminative-model approach is first considered, where an SQI map is directly trained using a paired dataset of CVS and its label [12, 22, 48]. Although this approach provides a high performance on a fixed dataset, owing to the class imbalance problem, there is a risk of overfitting on motion-influenced CVS data in the scope of generalization or stability [11, 15, 23, 52]. Motion artifacts can vary considerably in real circumstances, whereas collecting CVS data in numerous motion-influenced cases is practically limited because of the high cost, intensive labor, security, and ambiguity in clinical data acquisition and annotation

[13, 49, 53, 61]. To handle this conceivable difficulty, the manifold-learning approach [3, 25, 27, 31] is examined as an alternative. It does not learn irregular and capricious patterns of motion-influenced CVSs and only takes advantage of the learned features from motion-free CVSs.

Numerous experiments have been conducted using actual EIT data. Empirical results demonstrate that discriminative and manifold-learning models provide accurate and automatic detection of motion-influenced CVS in real-time. The best discriminative model achieved an accuracy of 0.95, positive and negative predictive values of 0.96 and 0.86, sensitivity of 0.98, specificity of 0.77, and AUC of 0.96. The best manifold-learning model achieved an accuracy of 0.93, positive and negative predictive values of 0.97 and 0.71, sensitivity of 0.95, specificity of 0.80, and AUC of 0.95. The discriminative models yielded a more powerful SQI performance; in contrast, the manifold-learning models provided stable outcomes between the training and test sets. Regarding to practical applications, the choice of two models relies on what should be emphasized in the monitoring system in terms of performance and stability.

2. Methods

This study considers the 16-channel system of the thoracic EIT, where 16 electrodes are attached along the human chest (see figure 2). The EIT system is assumed to be synchronized with the ECG system, which provides the time interval for each cardiac cycle. The EIT device measures a set of voltage differences by injecting an alternative current of I (mA) through pairs of adjacent electrodes while keeping all other electrodes insulated. At sampling time t , the following voltages are acquired:

$$\{V_t^{j,k} : V_t^{j,k} = U_t^{j,k} - U_t^{j,k+1}, j \in \mathcal{I}, k \in \mathcal{I} \setminus \{j, j+1\}\} \quad (1)$$

where \mathcal{I} is an index set defined by $\mathcal{I} = \{1, 2, \dots, 16\}$, \mathcal{E}_k is the k th electrode, and $U_t^{j,k}$ is the electrical potential on \mathcal{E}_k subject to the current injection from \mathcal{E}_j to \mathcal{E}_{j+1} . For notational convenience, \mathcal{E}^0 and \mathcal{E}^{17} can be understood as \mathcal{E}^{16} and \mathcal{E}^1 , respectively. Once the current is injected from \mathcal{E}^j to \mathcal{E}^{j+1} for some $j \in \mathcal{I}$, the voltage is measured at each of the 16 adjacent electrode pairs $(\mathcal{E}^k, \mathcal{E}^{k+1})_{k \in \mathcal{I}}$. Among the 16 voltages, $V_t^{j,j-1}$, $V_t^{j,j}$, and $V_t^{j,j+1}$ are discarded to reduce the influence of the skin-electrode contact impedance [47]. Because we perform 16 independent current injections, in total, 208 ($= 16 \times 13$) voltages are obtained and used to produce the CVS.

2.1. CVS extraction using EIT and influence of motion

A transconductance (column) vector $\mathbf{g}_t \in \mathbb{R}^{208}$ can be defined using the voltage data (1) as follows:

$$\mathbf{g}_t = \left[\frac{I}{\Re(V_t^{1,3})}, \dots, \frac{I}{\Re(V_t^{1,15})}, \dots, \frac{I}{\Re(V_t^{16,2})}, \dots, \frac{I}{\Re(V_t^{16,14})} \right]^T \quad (2)$$

where T represents the vector transpose and \Re is an operation for extracting the real part of a complex number. Here, \mathbf{g}_t is updated every 10 ms.

A CVS, denoted by $\mathbf{x}_t \in \mathbb{R}$, is obtained by

$$\mathbf{x}_t = \mathbf{w}^T \dot{\mathbf{g}}_t \quad (3)$$

where $\mathbf{w} \in \mathbb{R}^{208}$ is a weighting (so-called leadforming) vector and $\dot{\mathbf{g}}_t$ is time difference of \mathbf{g}_t given by

$$\dot{\mathbf{g}}_t = \mathbf{g}_t - \mathbf{g}_{t_0} \text{ for reference time } t_0 \quad (4)$$

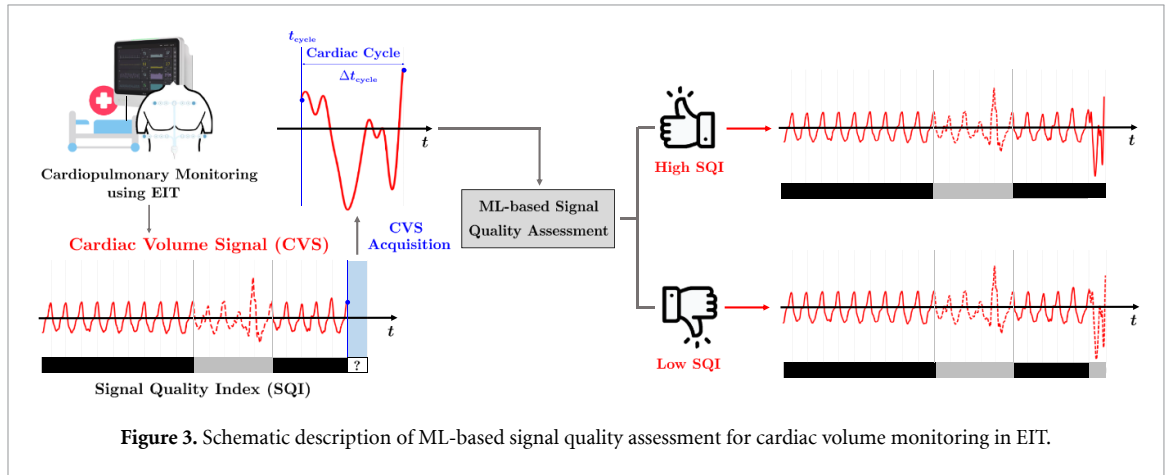
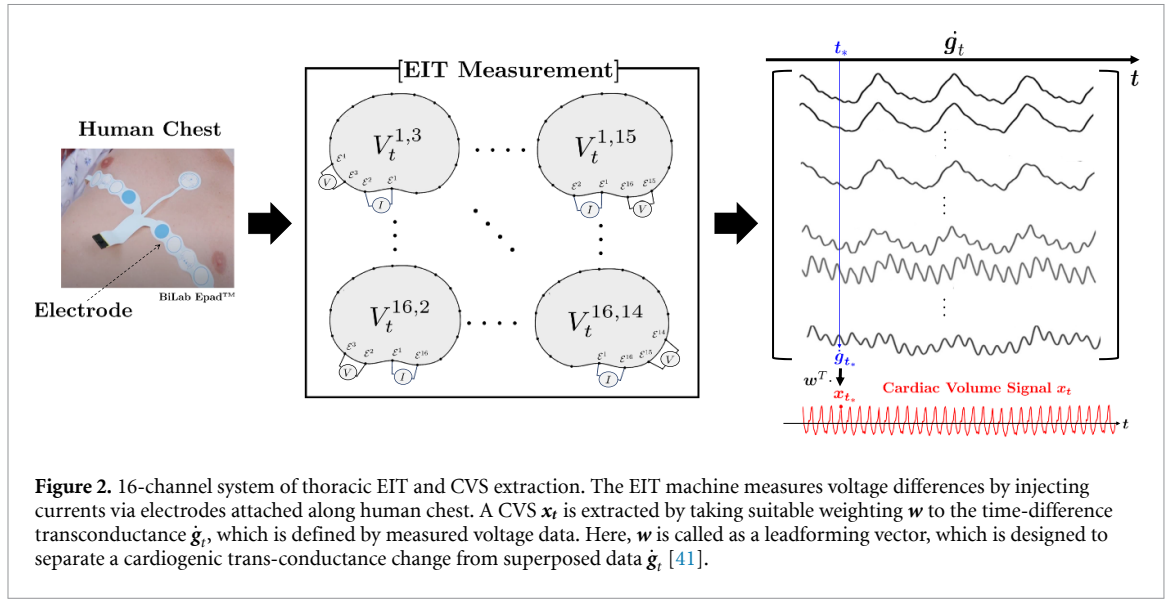
In the absence of motion, the transconductance $\dot{\mathbf{g}}_t$ can be expressed by

$$\dot{\mathbf{g}}_t = \dot{\mathbf{g}}_t^{\text{air}} + \dot{\mathbf{g}}_t^{\text{blood}} \quad (5)$$

where $\dot{\mathbf{g}}_t^{\text{air}}$ and $\dot{\mathbf{g}}_t^{\text{blood}}$ are transconductance vectors related to air and blood volume changes in the lungs and heart, respectively. The weighting vector \mathbf{w} is designed to provide

$$\mathbf{w}^T \dot{\mathbf{g}}_t = \mathbf{w}^T (\dot{\mathbf{g}}_t^{\text{air}} + \dot{\mathbf{g}}_t^{\text{blood}}) = \mathbf{w}^T \dot{\mathbf{g}}_t^{\text{blood}}. \quad (6)$$

See figure 2. Kindly refer to [41] for details on determining \mathbf{w} . Even though the cardiogenic signal $\dot{\mathbf{g}}_t^{\text{blood}}$ is weak, it can be accurately decomposed from the data \mathbf{g}_t .



In light of the previous analysis in [38], the following explains why the quality of the CVS is degraded by motion, as shown in the middle part of figure 1. In the presence of motion, the transconductance \dot{g}_t can be approximated by

$$\dot{g}_t \approx \dot{g}_t^{\text{normal}} + \dot{g}_t^{\text{motion}} \quad (7)$$

where $\dot{g}_t^{\text{normal}} = \dot{g}_t^{\text{air}} + \dot{g}_t^{\text{blood}}$ and $\dot{g}_t^{\text{motion}}$ is the motion-induced effect. Appendix A presents details of (7). Determining the vector w itself can be considerably affected by motion artifacts [41]. Moreover, even if w satisfies (6), we have

$$x_t = w^T \dot{g}_t \approx x_t^{\text{normal}} + x_t^{\text{motion}} \quad (8)$$

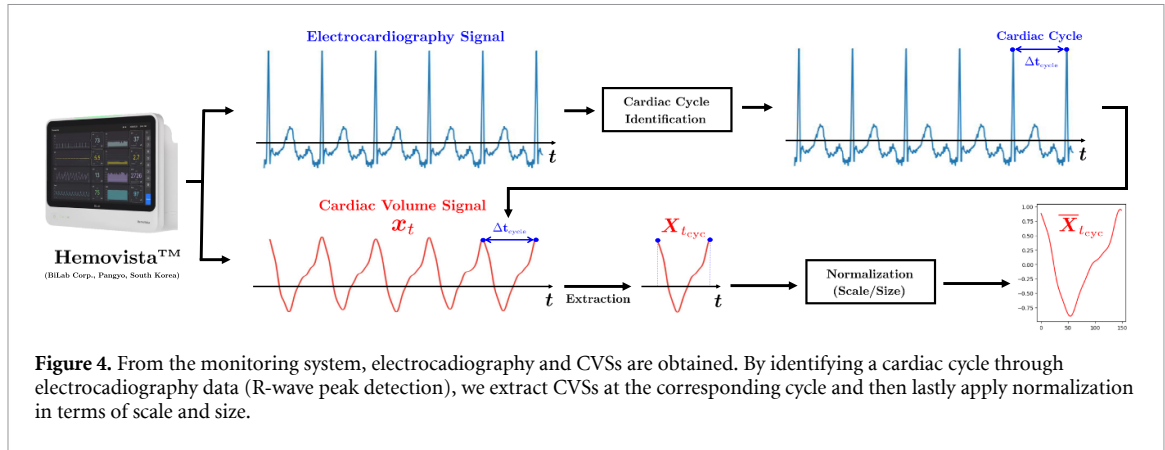
where $x_t^{\text{normal}} = w^T \dot{g}_t^{\text{blood}}$ and $x_t^{\text{motion}} = w^T \dot{g}_t^{\text{motion}}$. The last term x_t^{motion} describes motion artifacts in the CVS.

2.2. CVS quality assessment and data preprocessing

This study aims to assess the CVS (x_t) for detecting motion-induced signal quality degradation. See figure 3. This can be accomplished by developing an SQI map $f: x_t \mapsto y_t$ such that

$$f(x_t) = y_t = \begin{cases} 1 & \text{if } x_t^{\text{motion}} \approx 0 \\ 0 & \text{if } x_t^{\text{motion}} \not\approx 0. \end{cases} \quad (9)$$

However, it is arduous to achieve (9), where the assessment is conducted on an individual CVS at every sampling time. Instead, we take advantage of the periodicity and regularity of cardiac volume changes



according to the heartbeat. The time interval of each cardiac cycle is identified using a synchronized ECG system.

Our quality assessment is conducted on every cardiac cycle of CVS, where a cardiac cycle is defined by the time interval consisting of two consecutive ECG R-wave peaks as the end points. For a given time t_{cyc} , let the interval $[t_{cyc}, t_{cyc} + \Delta t_{cyc}]$ be the corresponding cardiac cycle, where Δt_{cyc} is assumed to be $\Delta t_{cyc} = 10\text{ms} \times (\nu - 1)$ for some $\nu \in \mathbb{N} \setminus \{1\}$. Here, \mathbb{N} denotes the set of positive integers. A vector gathering all CVSs during the cycle, denoted by $\mathbf{X}_{t_{cyc}} \in \mathbb{R}^\nu$, is defined as

$$\mathbf{X}_{t_{cyc}} = [\mathbf{x}_{t_{cyc}}, \mathbf{x}_{t_{cyc}+10\text{ms}}, \dots, \mathbf{x}_{t_{cyc}+10\text{ms} \times (\nu-1)}]^T. \quad (10)$$

The map f in (9) can be modified into

$$f(\mathbf{X}_{t_{cyc}}) = \mathbf{y}_t = \begin{cases} 1 & \text{for normal } \mathbf{X}_{t_{cyc}} \\ 0 & \text{for motion-influenced } \mathbf{X}_{t_{cyc}} \end{cases}. \quad (11)$$

To find f in (11), we leverage ML, which can learn the domain knowledge of normal and motion-influenced CVSs from a training dataset of N data pairs $\{\mathbf{X}^{(i)}, \mathbf{y}^{(i)}\}_{i=1}^N$. Prior to ML applications, the following issues need to be addressed in the CVS data. First, CVSs have significant inter-subject and intra-subject variability. This is because cardiac volume varies depending on various factors, including sex, age, condition, time, and body temperature. Therefore, scale normalization is required to enhance the stability and performance of ML while mitigating the high learning complexity associated with scale-invariant feature extraction [20, 56]. Second, the dimensions of the input CVS data in (11) do not match each other (i.e. ν is not constant) owing to heart rate variability [44]. Because most existing ML methods are based on an input with consistent dimensions, size normalization is required. Figure 4 schematically illustrates the overall process.

2.2.1. Scale normalization

A simple method of normalizing the scale is to rescale the CVS data for individual cardiac cycles. Specifically, for a given CVS vector $\mathbf{X}_{t_{cyc}} \in \mathbb{R}^\nu$, the scaling factor \mathcal{S} is obtained using

$$\mathcal{S} = \max_{i \in \mathcal{V}} |\mathbf{x}_{t_{cyc}+10 \times i(\text{ms})}| \quad (12)$$

where the index set \mathcal{V} is given by $\mathcal{V} = \{0, 1, \dots, \nu - 1\}$. Normalized CVS data, denoted by $\underline{\mathbf{X}}_{t_{cyc}}$, are obtained by

$$\underline{\mathbf{X}}_{t_{cyc}} = \frac{\mathbf{X}_{t_{cyc}}}{\mathcal{S}}. \quad (13)$$

However, this scaling may not be appropriate to our application for the following reason. Abnormalities in CVS data include sudden increases or decreases in signal amplitude as well as irregular deformations of the shape profile. The normalization in (13) can contribute to ignoring rapid amplitude changes.

This study uses the following subject-specific scale normalization strategy. When the EIT device is used to monitor a certain subject, it is supposed that during the initial 20 s calibration process, the device measures the normal CVS data available for scale normalization. Let $\mathcal{X}^{\text{subject}}$ be a set of corresponding CVSs given by

$$\mathcal{X}^{\text{subject}} = \{\mathbf{x}_{10 \times i(\text{ms})} : i = -1999, -1998, \dots, -1\}. \quad (14)$$

Using the set $\mathcal{X}^{\text{subject}}$, a subject-specific scaling factor $\mathcal{S}^{\text{subject}}$ is obtained by

$$\mathcal{S}^{\text{subject}} = \max_{\mathbf{x} \in \mathcal{X}^{\text{subject}}} |\mathbf{x}|. \quad (15)$$

This scale factor $\mathcal{S}^{\text{subject}}$ is used for the normalization in (13) instead of the naive factor \mathcal{S} in (12).

2.2.2. Size normalization

To make the dimensions of the CVS data consistent, a CVS vector $\mathbf{x}_{t_{\text{cyc}}}$ is embedded into \mathbb{R}^{ν} for a fixed constant ν . In the empirical experiment, the embedding space dimension was to be larger than any dimension of the CVS data in our dataset ($\nu = 150$).

Two normalization methods are considered. The first approach is to resample ν points using linear interpolation with ν data points in \mathbf{x}_t . For the stationary interval $[0, 1]$, the following linear interpolation function \mathcal{L} is constructed:

$$\mathcal{L}\left(\frac{i}{\nu-1}\right) = \mathbf{x}_{t_{\text{cyc}}+10(\text{ms}) \times (i-1)} \text{ for } i = 0, \dots, \nu-1. \quad (16)$$

Subsequently, we obtain the normalized vector $\bar{\mathbf{x}}_{t_{\text{cyc}}} \in \mathbb{R}^{\nu}$ using

$$\bar{\mathbf{x}}_{t_{\text{cyc}}} = \left[\mathcal{L}(0), \mathcal{L}\left(\frac{1}{\nu-1}\right), \mathcal{L}\left(\frac{2}{\nu-1}\right), \dots, \mathcal{L}(1) \right]^T. \quad (17)$$

This method normalizes the signal profile of CVS data into the desired length (ν) with no significant loss, but loses sampling time information. Second, the last value in $\mathbf{x}_{t_{\text{cyc}}}$ (i.e. $\mathbf{x}_{t_{\text{cyc}}+10(\text{ms}) \times (\nu-1)}$) is padded up to the desired length. This constant padding provides a vector $\bar{\mathbf{x}}_{t_{\text{cyc}}} \in \mathbb{R}^{\nu}$, expressed by

$$\bar{\mathbf{x}}_{t_{\text{cyc}}} = [\mathbf{x}_{t_{\text{cyc}}}, \dots, \mathbf{x}_{t_{\text{cyc}}+10(\text{ms}) \times (\nu-2)}, \mathbf{x}_{t_{\text{cyc}}+10(\text{ms}) \times (\nu-1)}, \quad (18)$$

$$\mathbf{x}_{t_{\text{cyc}}+10(\text{ms}) \times (\nu-1)}, \dots, \mathbf{x}_{t_{\text{cyc}}+10(\text{ms}) \times (\nu-1)}]^T \quad (19)$$

where the part (19) corresponds to the padding. In contrast to the first method, this normalization can preserve time information regarding sampling frequency, whereas the core profile of the CVS is supported at different time intervals.

2.3. ML application

At this point, we are ready to apply ML for determining the SQI function (11). Collected from various subjects and cardiac cycles, the following dataset is used:

$$\{\bar{\mathbf{X}}^{(i)}, \mathbf{y}^{(i)}\}_{i=1}^N \quad (20)$$

where $\mathbf{y}^{(i)}$ is the SQI label corresponding to $\bar{\mathbf{X}}^{(i)}$. We note that $\bar{\mathbf{X}}$ is the CVS data for a cardiac cycle of some subjects and is normalized for both scale and size. In practice, the available training dataset (20) was highly imbalanced, where there were relatively few negative samples (motion-influenced CVSs).

2.3.1. Discriminative-model approach

The discriminative-model approach trains the SQI map $f: \bar{\mathbf{X}} \mapsto \mathbf{y}$ in the following sense:

$$f = \underset{f \in \mathbb{F}}{\operatorname{argmin}} \frac{1}{N} \sum_{i=1}^N \operatorname{dist}(f(\bar{\mathbf{X}}^{(i)}), \mathbf{y}^{(i)}) \quad (21)$$

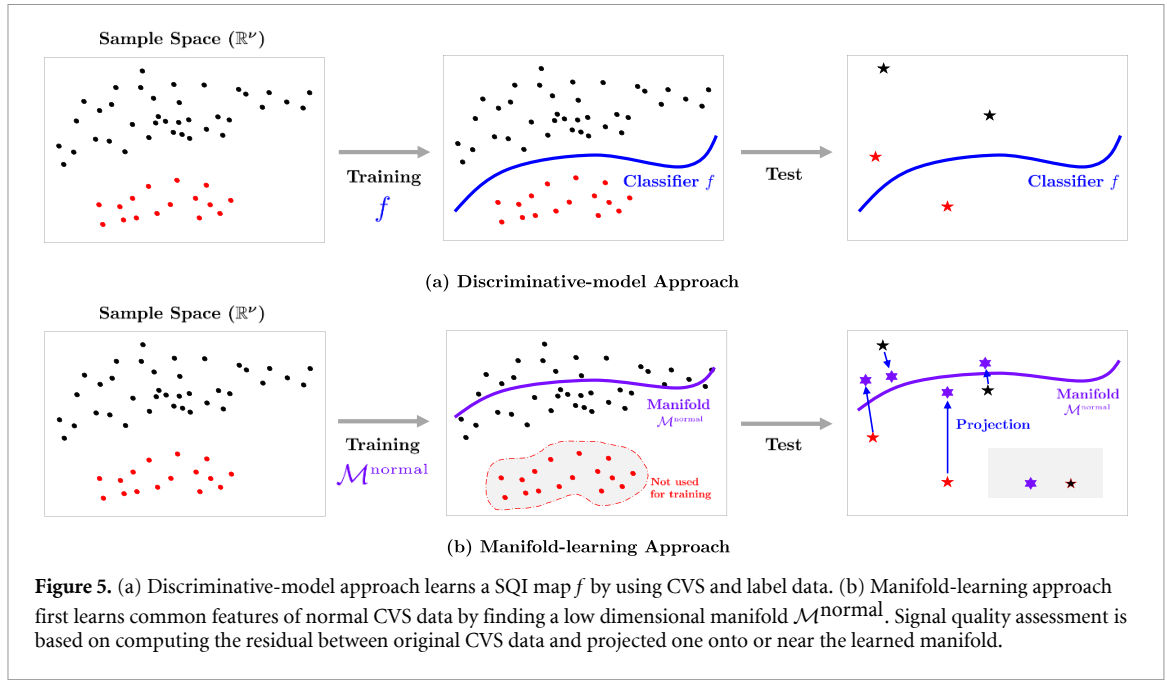


Figure 5. (a) Discriminative-model approach learns a SQI map f by using CVS and label data. (b) Manifold-learning approach first learns common features of normal CVS data by finding a low dimensional manifold $\mathcal{M}^{\text{normal}}$. Signal quality assessment is based on computing the residual between original CVS data and projected one onto or near the learned manifold.

where \mathbb{F} is a set of learnable functions for a given ML model and dist is a metric that measures the difference between the ML output $f(\bar{\mathbf{X}})$ and label \mathbf{y} . See figure 5(a). In our application with high class-imbalance, the following weighted cross-entropy can be used:

$$\text{dist}(f(\bar{\mathbf{X}}), \mathbf{y}) = -\zeta_{\text{pos}} \mathbf{y} \log(f(\bar{\mathbf{X}})) - \zeta_{\text{neg}} (1 - \mathbf{y}) \log(1 - f(\bar{\mathbf{X}})) \quad (22)$$

where ζ_{pos} and ζ_{neg} are the relative ratios of the positive and negative samples, respectively. Various classification models can be used, such as the logistic regression model (LR) [12], multi-layer perceptron (MLP) [22], and convolutional neural networks (CNNs) [48]. Detailed models used in this study are explained in appendix B.1.

The discriminative model approach is a powerful method to guarantee high performance in a fixed dataset. However, it might suffer from providing stable SQI results in clinical practice because of highly variable negative samples. This is because these methods take advantage of learned information using only a few negative samples [11, 15, 23, 52]. To achieve stable prediction, the manifold-learning approach can be alternatively used [13, 53, 61].

2.3.2. Manifold-learning approach

The manifold-learning approach learns common features from positive samples (i.e. normal CVS) and uses them to develop an SQI map. The remaining negative samples are utilized as auxiliary means for selecting a hyperparameter. Figure 5(b) shows a schematic description of this process.

A set of positive samples is denoted by $\{\bar{\mathbf{X}}_{\text{pos}}^{(i)}\}_{i=1}^{N_{\text{pos}}}$, where N_{pos} denotes the number of positive samples. In the first step, we learn a low-dimensional representation of $\bar{\mathbf{X}}_{\text{pos}}$ by training an encoder $\mathcal{E} : \bar{\mathbf{X}}_{\text{pos}} \mapsto \mathbf{z}$ and decoder $\mathcal{D} : \mathbf{z} \mapsto \bar{\mathbf{X}}_{\text{pos}}$ in the following sense [21, 27]:

$$(\mathcal{D}, \mathcal{E}) = \underset{(\mathcal{D}, \mathcal{E})}{\text{argmin}} \frac{1}{N_{\text{pos}}} \sum_{i=1}^{N_{\text{pos}}} \|\mathcal{D} \circ \mathcal{E}(\bar{\mathbf{X}}_{\text{pos}}^{(i)}) - \bar{\mathbf{X}}_{\text{pos}}^{(i)}\|_2^2 \quad (23)$$

where \mathbf{z} is a low dimensional latent vector and $\|\cdot\|_2$ is the standard Euclidean norm. The architectures \mathcal{D} and \mathcal{E} can be used in PCA [27], VAE [31], and β -VAE [25]. See more details in appendix B.2.

Borrowing the idea from [3], an SQI map f is constructed as follows: For a given CVS data $\bar{\mathbf{X}}$ in any class, a residual \mathbf{r} is computed by

$$\mathbf{r} = \|\bar{\mathbf{X}} - \mathcal{D} \circ \mathcal{E}(\bar{\mathbf{X}})\|_2. \quad (24)$$

The decoder \mathcal{D} is trained to generate normal CVS-like output. In other words, operation $\mathcal{D} \circ \mathcal{E}$ transforms $\bar{\mathbf{X}}$ to lie in or near the learned manifold using normal CVS data [47, 58]. Therefore, the residual \mathbf{r} can be viewed

as an anomaly score, where r is small if \bar{X} is normal CVS data, and large if \bar{X} is motion-influenced CVS data. For some non-negative constant d , an SQI map f can be constructed using

$$f(\bar{X}_t) = \begin{cases} 1 & \text{if } r \leq d \\ 0 & \text{if } r > d \end{cases} \quad (25)$$

The remainder of this subsection explains how the thresholding value d is determined by utilizing negative samples as well as positive. By varying d from 0 to ∞ , a receiver operating characteristic (ROC) curve is calculated, where a point in the ROC curve is obtained using a fixed d . We choose d such that maximizing Youden's J statistics, which is known as an unbiased metric in the class imbalance case [45]. The value J is given by

$$J^d = \text{Sensitivity}^d + \text{Specificity}^d - 1 \quad (26)$$

where

$$\text{Sensitivity}^d = \frac{N_{TP}^d}{N_{TP}^d + N_{FN}^d} \text{ and } \text{Specificity}^d = \frac{N_{TN}^d}{N_{TN}^d + N_{FP}^d}. \quad (27)$$

Here, N_{TP}^d , N_{TN}^d , N_{FP}^d , and N_{FN}^d respectively represent the number of true positives, true negatives, false positives, and false negatives for predictions depending on a selected threshold value d . See appendix B.2.4.

3. Results

3.1. Data acquisition and experimental setting

Our dataset was obtained from healthy volunteers using an EIT-based hemodynamic monitoring device (HemoVista, BiLab, South Korea). Synchronized ECG data were obtained with EIT and used to identify the cardiac cycles. While lying in a hospital bed, each subject was requested to make intentional motions mimicking postural changes in the clinical ward. A total of 16 140 CVS data were obtained regarding the cardiac cycle.

Manual labeling was individually performed by two- and ten- years bio-signal experts (Nam and Lee). Subsequently, they reviewed the results and made the final decision about CVS abnormality through an agreement between them. The final labels were annotated into three classes: normal, ambiguous, and motion-influenced. When classified as normal or abnormal by both experts with an agreement, CVS data were annotated as normal or motion-influenced classes. The ambiguous class stands for CVS data in which motion artifacts were included with high possibility, but the experts did not reach an explicit agreement about motion influence. The assigned label is $y = 1$ for the normal class and $y = 0$ for the other classes. As a result, 12 928 (80.09%), 1526 (9.45%), and 1686 (10.45%) samples were labeled as normal, ambiguous, and motion-influenced classes, respectively.

For ML applications, a total of 16 372 CVS data were divided into 13 100 (80%), 1520 (10%), and 1520 (10%), which were used for training, validation, and testing, respectively. The data split was performed such that CVS data obtained from a common subject did not exist between the three sets. For the training dataset, labels for the ambiguous class were reassigned to $y = 0.25$. This was done to prevent the over-classification of ambiguous classes.

ML experiments were conducted in a computer system with GeForce RTX 3080 Ti, Intel® Core™ X-series Processors i9-10 900X, and 128GB DDR4 RAM. Python with scikit-learn and Pytorch packages were used for the ML implementation. When training the ML models, the Adam optimizer was consistently employed, which is an effective adaptive stochastic gradient descent method [32]. Hyperparameters such as epoch and learning rate were heuristically chosen based on the validation results. See details in appendix B.3.

3.2. Results of CVS quality assessment

We compared the performance of the ML-based CVS quality assessment results by using six metrics: accuracy, positive and negative predictive values (PPV and NPV), sensitivity, specificity, and AUC. Accuracy, PPV, and NPV were defined by

$$\text{Accuracy} = \frac{N_{TP} + N_{TN}}{N_{TP} + N_{TN} + N_{FP} + N_{FN}}, \text{PPV} = \frac{N_{TP}}{N_{TP} + N_{FP}}, \text{ and } \text{NPV} = \frac{N_{TN}}{N_{TN} + N_{FN}} \quad (28)$$

and AUC was the area under the ROC curve. NPV, specificity, and AUC should be emphasized in our evaluation owing to the high-class imbalance (small negative samples).

Table 1. ML-based CVS quality assessment results.

(a) SQI with scale and size normalization using linear interpolation.							
Discriminative Model		LR	MLP1	MLP2	VGG16-3	VGG16-4	VGG16-5
Test	Accuracy	0.8665	0.9323	0.9348	0.9468	0.9468	0.9437
	PPV	1.0000	0.9790	0.9747	0.9525	0.9605	0.9679
	NPV	0.1097	0.7241	0.7445	0.9047	0.8591	0.8083
	Sensitivity	0.8643	0.9404	0.9479	0.9866	0.9776	0.9657
	Specificity	1.0000	0.8860	0.8607	0.7215	0.7721	0.8185
	AUC	0.6615	0.9506	0.9558	0.9709	0.9645	0.9653
Manifold-learning Model		PCA	VAE	β -VAE	CVAE	β -CVAE	—
Test	Accuracy	0.8468	0.9066	0.9221	0.9292	0.9298	
	PPV	0.9510	0.9687	0.9672	0.9688	0.9739	
	NPV	0.4573	0.6181	0.6900	0.7100	0.7011	
	Sensitivity	0.8675	0.9218	0.9439	0.9486	0.9441	—
	Specificity	0.7142	0.8095	0.7952	0.8047	0.8380	
	AUC	0.8735	0.9513	0.9489	0.9528	0.9603	
(b) SQI with scale and size normalization using constant padding.							
Discriminative Model		LR	MLP1	MLP2	VGG16-3	VGG16-4	VGG16-5
Test	Accuracy	0.8664	0.9487	0.9518	0.9455	0.9487	0.9500
	PPV	1.0000	0.9745	0.9767	0.9533	0.9655	0.9731
	NPV	0.0826	0.7851	0.8065	0.8870	0.8433	0.8185
	Sensitivity	0.8648	0.9651	0.9666	0.9844	0.9748	0.9681
	Specificity	1.0000	0.8521	0.8652	0.7173	0.7956	0.8434
	AUC	0.6628	0.9725	0.9669	0.9782	0.9683	0.9757
Manifold-learning Model		PCA	VAE	β -VAE	CVAE	β -CVAE	—
Test	Accuracy	0.8809	0.8918	0.9214	0.9015	0.8861	
	PPV	0.9590	0.9660	0.9679	0.9731	0.9636	
	NPV	0.5333	0.5629	0.6694	0.5882	0.5467	
	Sensitivity	0.9014	0.9074	0.9407	0.9118	0.9029	—
	Specificity	0.7450	0.7892	0.7941	0.8333	0.7745	
	AUC	0.9150	0.9206	0.9412	0.9170	0.9041	

3.2.1. Discriminative models

The first and second rows of tables 1(a) and (b) show the quantitative evaluations of CVS quality assessment using various discriminative models: LR, MLPs, and CNNs. The results in tables 1(a) and (b) differ in size normalization: (a) linear interpolation and (b) constant padding.

MLPs and CNNs performed better than LR, which provided miserable NPV and AUC. MLPs and CNNs outperformed each other in specificity and NVP respectively, while achieving comparable levels for the other metrics. There was no significant performance gap depending on the size normalization.

One interesting observation was as follows: In our experiments, there seems to be a compensation between specificity and NPV, depending on the emphasis on locality and globality. Enriching global information on CVS data positively affected specificity; in contrast, local information helped improve NPV. As the receptive field size in VGG16 increased (see appendix B.1), specificity tended to increase and NPV decrease. In MLP, which is more flexible for catching global information than CNNs, specificity was highest, and NPV lowest. In other words, the local information of CVS data is likely to play a crucial role in reducing false negatives rather than false positives. From a practical point of view, reducing false negatives is more desirable; therefore, using VGG16-3 or VGG16-4, which have the powerful ability to take advantage of locality, can be an excellent option.

3.2.2. Manifold-learning models

Positive samples in the validation set were used for hyperparameter selection in training the encoder and decoder. A threshold value was determined by using data from all the training and validation sets.

Figure 6 shows manifold projection results of test samples in normal and motion-influenced classes. An input CVS is projected onto or near a manifold learned by positive samples. As desired, the residual (24) tends to be small for normal samples and high for motion-influenced samples.

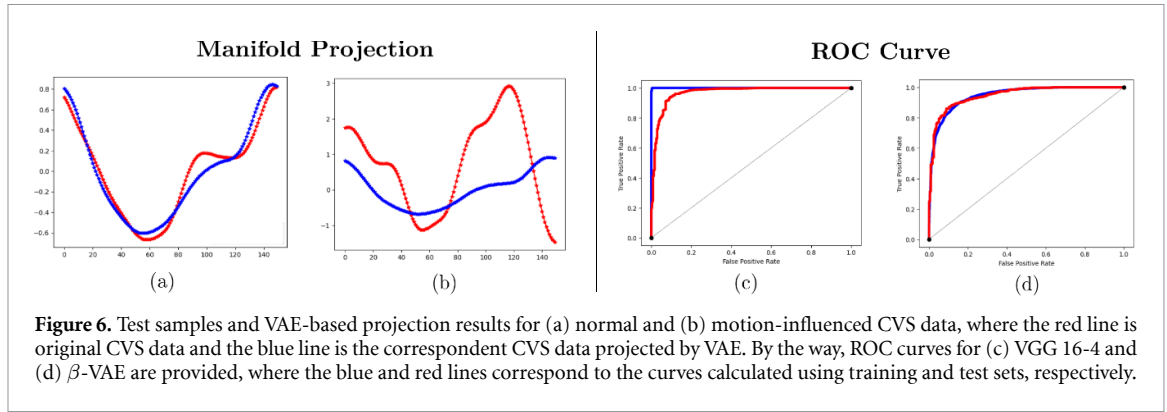


Figure 6. Test samples and VAE-based projection results for (a) normal and (b) motion-influenced CVS data, where the red line is original CVS data and the blue line is the correspondent CVS data projected by VAE. By the way, ROC curves for (c) VGG 16-4 and (d) β -VAE are provided, where the blue and red lines correspond to the curves calculated using training and test sets, respectively.

Table 2. Results of ML-based CVS quality assessment with and without scale normalization.

Model	With Scaling		Without Scaling	
	VGG16-3	VAE	VGG16-3	VAE
Accuracy	0.9468	0.9066	0.7862	0.7509
PPV	0.9525	0.9687	0.9763	0.9668
NPV	0.9047	0.6181	0.4038	0.3327
Sensitivity	0.9886	0.9218	0.7671	0.7373
Specificity	0.7215	0.8095	0.8945	0.8380
AUC	0.9709	0.9513	0.9067	0.8906

The third and fourth rows of tables 1(a) and (b) show the final assessment results using manifold-learning models. The performance was comparable to that of discriminative models. We note that the manifold-learning models never learned negative samples for classifier development. As shown in figure 6(d), the manifold-learning model's performance gap between training and test sets was very small.

There was a slight difference in performance for the manifold-learning models depending on the size normalization. Linear interpolation promised a slightly better assessment of accuracy, NPV, and AUC than the other. For the case of constant padding, because core profiles of CVS data are supported at different intervals, the learning complexity can be increased, which is associated with invariant feature extraction to the intervals. This may cause a slight drop in performance.

In our dataset, both discriminative and manifold learning models provided accurate detection of motion-influenced CVS. The discriminative model yielded a more powerful SQI performance; in contrast, the manifold-learning model provided stable outcomes between the training and test sets. Regarding practical applications, the choice of two models relies on what should be emphasized in the monitoring system in terms of performance and stability. Their ensemble is also worth considering.

To be precise, by taking advantage of both discriminative and manifold-learning models, one may design an efficient warning system for motion-corruption. A specific example is as follows: Let $\mathcal{W}_{\text{warning}}$ be a warning system. The following three-level warning system can be designed: For given CVS data \bar{X} ,

$$\mathcal{W}_{\text{warning}}(\bar{X}) = \begin{cases} \text{normality} & \text{if } f_{\text{disc}}(\bar{X}) = f_{\text{mani}}(\bar{X}) = 1, \\ \text{caution} & \text{if } f_{\text{disc}}(\bar{X}) \neq f_{\text{mani}}(\bar{X}), \\ \text{warning} & \text{if } f_{\text{disc}}(\bar{X}) = f_{\text{mani}}(\bar{X}) = 0, \end{cases} \quad (29)$$

where f_{disc} and f_{mani} are learned discriminative and manifold-learning models. In the case that f_{disc} and f_{mani} provide a consistent assessment, the warning system $\mathcal{W}_{\text{warning}}$ gives clear normality or warning about CVS corruption. When providing an inconsistent result, the system $\mathcal{W}_{\text{warning}}$ gives a caution that motion corruption may exist. This can be viewed as an agreement between two independent observers f_{disc} and f_{mani} , which resembles the manual assessment mentioned in section 3.1. This warning system may be more flexible for the practical use rather than directly serving the assessment based on the individual use of f_{disc} or f_{mani} .

3.2.3. Impact of scale normalization

Table 2 shows the worst case when scale normalization was not applied. In CNNs, network training was very unstable, and assessment performance was considerably degraded, especially regarding accuracy, NPV, sensitivity, and AUC. In VAEs, large-scale variability of CVS data highly affected the loss of accuracy in

Table 3. Test inference time of ML-based CVS quality assessment methods.

Model	LR	MLP1	MLP2	VGG16-3	VGG16-4
Time	1.61 μ s	8.34 μ s	2.32 μ s	31.49 μ s	33.71 μ s
Model	VGG16-5	PCA	VAE	CVAE	—
Time	44.48 μ s	14.99 μ s	15.38 μ s	57.61 μ s	—

manifold projection; therefore, the performance significantly deteriorated in terms of accuracy, NPV, sensitivity, and AUC. This verifies the impact of scale normalization.

3.2.4. Inference time

In real-time monitoring, assessment should be performed quickly. The input for the proposed method was updated for every heartbeat in the EIT system. Assuming a subject with a constant 80bpm, the CVS input is updated every 0.75 s. Roughly, the assessment should be faster than approximately 10^{-2} s. Table 3 shows the inference time for the test data, calculated by taking the average over the entire test data. After training a network with the GPU system, we evaluated the inference time by using the CPU system in a laptop environment (SurfacePro7 equipped with Intel(R) Core(TM) Processors i5-1035G4 and 8GB DDR4 RAM), which is at a similar level to an EIT monitoring device. The ML models provided a test outcome with inference time between 1 μ s (10^{-6} s) and 100 μ s (10^{-3} s). This confirms that the proposed method meets the speed requirements for real-time monitoring.

4. Conclusion and discussion

We developed a novel automated SQI method using two ML techniques, the discriminative model and manifold learning, to detect abnormal CVS caused by motion-induced artifacts. We discussed how body movement influences the transconductance data and how the resulting CVS is degraded by movement. Numerous experiments support the idea that the proposed method can successfully filter motion-induced unrealistic variations in CVS data.

To the best of our knowledge, this is the first attempt to assess CVS quality to enhance the clinical capability of an EIT-based cardiopulmonary monitoring system. From a practical point of view, the proposed method can alert clinicians about CVS corruption to minimize misinformation about patient safety and facilitate adequate management of patients and medical resources. The proposed method can be combined with a software system for existing EIT devices.

The proposed method leverages the scale and size normalization before applying the ML techniques. The scale normalization is based on the subject-specific scaling factor, which is derived from the assumption that normal CVSs are obtained during initial 20 s of EIT measurement. In practice, we can take advantage of the existing calibration process that is typically conducted whenever a monitoring device is installed to a specific subject. In the calibration stage, a subject is asked to temporally be in postural restriction and then the monitoring device checks and tunes EIT parameters while acquiring normal data. Accordingly, these normal EIT data are available to compute the scale factor. Occasionally, it is probable to experience unexpected movements such as seizures during the calibration, which cause to measure erroneous data possibly resulting in the inappropriate scale normalization. In this case, it is needed to perform the calibration process again for preventing the ineffectiveness or performance degradation. Meanwhile, once the factor is determined, it is applied as the simple multiplication (13) and, thus, does not considerably affect on the timeliness of the proposed method.

There are various approaches to decide the cut-point d with numerous metrics such as accuracy, Youden's J statistics, index of union, and so on [35]. In this application, the use of the Youden's J statistics as a cut-off-value decision criterion can be a good choice, because the class imbalance is one of the core issues. The metric J is known to provide a meaningful statistics even for a class imbalanced dataset and has the strong relationship with the ROC curve [2, 24, 45]. However, it may not be optimal in the practical perspective that puts the relative emphasis on sensitivity (reducing false negatives) rather than specificity (reducing false positives). To deal with this, several sensitivity-focused strategies such as weighted J can be taken into account, but their effectiveness or optimality should be carefully investigated and validated in the practical environment with the feedback of monitoring device users. This is a subject of our future research.

The use of only healthy subject data in the training process did not fully consider possible influence of the subject's illness on CVS. SQI performance might be degraded in patients with illnesses such as arrhythmias, in which irregular deformation may occur in CVS due to premature ventricular contraction and lead to be classified as low signal quality. However, when ill patient data are available and appended in the training

process, a slightly modified SQI can detect the illness and motion by adding another label class. Meanwhile, arrhythmia can be easily detected using ECG signals.

A further collection of CVS data could be a strategy for enhancing model generalization or stability toward being equipped with an actual monitoring system. In discriminative models, even with additional data collection, generalization or stability might not be meaningfully improved because the class imbalance problem remains or increases. In contrast, the manifold-learning models can accurately infer common features (i.e. data manifolds) as the total number of normal CVS data grows regardless of class imbalance. In addition, it can be extended into a semi-supervised or unsupervised learning framework [3, 49], which reduces the requirement for labeled datasets. Thus, manifold-learning models might be favorable.

Data availability statement

The data cannot be made publicly available upon publication because they contain commercially sensitive information. The data that support the findings of this study are available upon reasonable request from the authors.

Acknowledgments

This work was supported by the Ministry of Trade, Industry and Energy (MOTIE) in Korea through the Industrial Strategic Technology Development Program under Grant 20006024. We are deeply grateful to BiLab (Pangyo, South Korea) for their help and collaboration.

Conflict of Interest

The authors have no conflicts to disclose.

Appendix A. Motion-induced effect on trans-conductance

In the 16 channel EIT system, the voltage data $\{V_t^{j,k}\}_{j,k}$ in (1) are governed by the following complete electrode model [47]: At time t , the electric potential distribution (u_t^j) and electric potential on an electrode ($U_t^{j,k}$) satisfy

$$\left\{ \begin{array}{l} \nabla \cdot (\gamma_t \nabla u_t^j) = 0 \quad \text{in } \Omega \subset \mathbb{R}^3 \\ \gamma_t \nabla u_t^j \cdot n = 0 \quad \text{on } \partial\Omega \setminus \bigcup_i^{16} \mathcal{E}^k \\ \int_{\mathcal{E}^k} \gamma_t \nabla u_t^j \cdot n = 0 \quad \text{for } k \in \mathcal{I} \setminus \{j, j+1\} \\ u_t^j + z_k (\gamma_t \nabla u_t^j \cdot n) = U_t^{j,k} \text{ on } \mathcal{E}^k \text{ for } k \in \mathcal{I} \\ \int_{\mathcal{E}^j} \gamma_t \nabla u_t^j \cdot n ds = - \int_{\mathcal{E}^{j+1}} \gamma_t \nabla u_t^j \cdot n ds = I \end{array} \right. \quad (\text{A.1})$$

where γ_t is a conductivity distribution in a human chest Ω at t , n is a unit normal vector outward $\partial\Omega$, ds is a surface element, and z_k is a skin-electrode contact impedance on \mathcal{E}^k . The amount of electric current I , which is injected to the domain Ω , can be scaled and thus assumed to be $I = 1$.

In the case that the human chest Ω is time-varying owing to motions, Reynolds transport theorem yields the following approximation [41]:

$$\dot{V}_t^{j,k} \approx \dot{V}_t^{j,k,\text{normal}} + \dot{V}_t^{j,k,\text{motion}} \quad (\text{A.2})$$

where

$$\dot{V}_t^{j,k,\text{normal}} = - \int_{\Omega} \dot{\gamma}_t(\mathbf{r}) \nabla u_t^j(\mathbf{r}) \cdot \nabla u_t^k(\mathbf{r}) d\mathbf{r} \quad (\text{A.3})$$

$$\dot{V}_t^{j,k,\text{motion}} = - \int_{\partial\Omega} \mathbf{v}_n(\mathbf{r}, t) \gamma_t(\mathbf{r}) \nabla u_t^j(\mathbf{r}) \cdot \nabla u_t^k(\mathbf{r}) ds. \quad (\text{A.4})$$

Here, \mathbf{v}_n is an outward-normal directional velocity of $\partial\Omega$ and $\mathbf{r} \in \Omega$ is a position vector in Ω . The term $\dot{V}_t^{j,k,\text{normal}}$ and $\dot{V}_t^{j,k,\text{motion}}$ can be viewed as voltage data acquirable in normal EIT measurement and motion-induced inference, respectively.

A similar relation to (A.2) for trans-conductance can be derived as follows: Let us define a trans-conductance-related value $g_t^{j,k}$ by

$$g_t^{j,k} = \frac{I}{\Re(V_t^{j,k})}. \quad (\text{A.5})$$

By differentiating $g_t^{j,k}$ with respect to t , we obtain

$$\dot{g}_t^{j,k} = \frac{-\Re(\dot{V}_t^{j,k})}{\left(\Re(V_t^{j,k})\right)^2} \approx \frac{-I \left(\Re(\dot{V}_t^{j,k,\text{normal}}) + \Re(\dot{V}_t^{j,k,\text{motion}}) \right)}{\left(\Re(V_t^{j,k})\right)^2}. \quad (\text{A.6})$$

The approximation (A.6) can be expressed as

$$\dot{g}_t^{j,k} \approx \dot{g}_t^{j,k,\text{normal}} + \dot{g}_t^{j,k,\text{motion}} \quad (\text{A.7})$$

where

$$\dot{g}_t^{j,k,\text{normal}} = \frac{-\Re(\dot{V}_t^{j,k,\text{normal}})}{\left(\Re(V_t^{j,k})\right)^2} \text{ and } \dot{g}_t^{j,k,\text{motion}} = \frac{-\Re(\dot{V}_t^{j,k,\text{motion}})}{\left(\Re(V_t^{j,k})\right)^2}. \quad (\text{A.8})$$

We note that, in the case of $\mathbf{v}_n = \mathbf{0}$ in (A.4) (i.e. EIT measurement is not affected by motions), the relation (A.6) becomes $\dot{g}_t^{j,k} = \dot{g}_t^{j,k,\text{normal}}$ by the reason of $\dot{V}_t^{j,k,\text{motion}} = 0$. In the form of trans-conductance vector, the following approximation holds:

$$\dot{\mathbf{g}}_t \approx \dot{\mathbf{g}}_t^{\text{normal}} + \dot{\mathbf{g}}_t^{\text{motion}} \quad (\text{A.9})$$

where

$$\dot{\mathbf{g}}_t^{\text{normal}} = [\dot{g}_t^{1,3,\text{normal}}, \dots, \dot{g}_t^{16,14,\text{normal}}] \text{ and } \dot{\mathbf{g}}_t^{\text{motion}} = [\dot{g}_t^{1,3,\text{motion}}, \dots, \dot{g}_t^{16,14,\text{motion}}]. \quad (\text{A.10})$$

If $\dot{\mathbf{g}}_t^{\text{normal}}$ satisfies the relation (5), we consequently obtain

$$\dot{\mathbf{g}}_t \approx \dot{\mathbf{g}}_t^{\text{air}} + \dot{\mathbf{g}}_t^{\text{blood}} + \dot{\mathbf{g}}_t^{\text{motion}}. \quad (\text{A.11})$$

Here, we note that $\dot{\mathbf{g}}_t^{\text{motion}}$ becomes more significant as motion (i.e. $|\mathbf{v}_n|$ in (A.4)) is large.

Appendix B. Machine learning models

B.1. Discriminative models

B.1.1. Logistic regression (LR)

A LR model f_{LR} consists of linear transformation and sigmoid as follows:

$$f_{\text{LR}}(\bar{\mathbf{X}}) = \sigma(\mathbf{w}^T \bar{\mathbf{X}} + b) \quad (\text{B.1})$$

where $\mathbf{w} \in \mathbb{R}^{150}$ and $b \in \mathbb{R}$ are learnable weight and bias, and σ is a sigmoid function given by $\sigma(x) = (1 + \exp(-x))^{-1}$.

B.1.2. Multilayer perceptron (MLP)

A MLP model f_{MLP} has a hierarchical structure with nonlinearity compared to LR. Each layer consists of linear transformation and nonlinear activation. In our MLP models, ReLU is used in all layers except the last to avoid gradient vanishing [20]. Table B1 shows the architectures of the MLPs used in this study.

B.1.3. CNN

A CNN model f_{CNN} consists of two paths; (1) feature extraction and (2) classification paths. In this study, the feature extraction path is based on VGG16 [48], as shown in table B1. The resultant feature map is flattened and then forwarded to the classification path, which is a MLP.

The feature extraction path is a series of two convolutional and maxpooling (or flatten) layers, whose depth is associated with receptive field (RF) size of a unit in the last convolutional layer [37]. According to the length of this series, VGG16-3, -4, and -5 are defined, where 3, 4, and 5 represent the iteration number of the layers in the series. Here, RFs are given by 32, 68, and 140, respectively.

Table B1. Network architectures; MLP and VGG.

(a) MLP1 (MLP2)						
Layer	Input Dim		Output Dim		Activation	
Linear	150	(150)	150	(150)	ReLU	
Linear	150	(150)	300	(150)	ReLU	
Linear	300	(150)	300	(100)	ReLU	
Linear	300	(100)	150	(50)	ReLU	
Linear	150	(50)	150	(25)	ReLU	
Linear	150	(25)	150	(10)	ReLU	
Linear	150	(10)	1	(1)	Sigmoid	
(b) VGG16-5; [1] Feature extraction and [2] Classification networks						
	Layer	Input Dim	Output Dim	Kernel	Activation	RF
[1]	Conv1D	150×1	150×4	3×4	ReLU	3
	Conv1D	150×4	150×4	3×4	ReLU	5
	MaxPool1D	150×4	75×4	2	ReLU	6
	Conv1D	75×4	75×8	3×8	ReLU	10
	Conv1D	75×8	75×8	3×8	ReLU	14
	MaxPool1D	75×8	37×8	2	ReLU	16
	Conv1D	37×8	37×16	3×16	ReLU	24
	Conv1D	37×16	37×16	3×16	ReLU	32
	MaxPool1D	37×16	18×16	2	ReLU	36
	Conv1D	18×16	18×32	3×32	ReLU	52
	Conv1D	18×32	18×32	3×32	ReLU	68
	MaxPool1D	18×32	9×32	2	ReLU	76
	Conv1D	9×32	9×64	3×64	ReLU	108
	Conv1D	9×64	9×64	3×64	ReLU	140
		Flatten	9×64	576×1	—	—
[2]	Linear	576×1	576×1	—	ReLU	—
	Linear	576×1	1×1	—	Sigmoid	—

B.2. Manifold-learning models

This subsection explains structures of an encoder \mathcal{E} and a decoder \mathcal{D} in (23), which were used for the manifold-learning approach described in section 2.3.2. The dimension of the latent vector \mathbf{z} was constantly set as 10 in our experiments.

B.2.1. Principal component analysis (PCA)

PCA learns principal vectors $\{\mathbf{v}_i \in \mathbb{R}^{150}\}_{i=1}^{10}$ in the following sense: For $i = 1, \dots, 10$,

$$\mathbf{v}_i = \underset{\|\mathbf{v}\|=1}{\operatorname{argmax}} \|\mathfrak{X}_i \mathbf{v}\|_2^2 \text{ and } \mathfrak{X}_i = \mathfrak{X}_{i-1} - \mathbf{v}_{i-1} \mathbf{v}_{i-1}^T \quad (\text{B.2})$$

where $\mathfrak{X}_1 := [\bar{\mathbf{X}}_{\text{pos}}^{(1)}, \bar{\mathbf{X}}_{\text{pos}}^{(2)}, \dots, \bar{\mathbf{X}}_{\text{pos}}^{(N_{\text{pos}})}]^T$. For ease of explanation, \mathfrak{X}_1 is assumed to be zero-mean. An encoder \mathcal{E}_{pca} and a decoder \mathcal{D}_{pca} are given by

$$\mathcal{E}_{\text{pca}}(\bar{\mathbf{X}}) = \mathbf{z} := [\langle \bar{\mathbf{X}}, \mathbf{v}_1 \rangle, \dots, \langle \bar{\mathbf{X}}, \mathbf{v}_{10} \rangle] \text{ and } \mathcal{D}_{\text{pca}}(\mathbf{z}) = \sum_{j=1}^{10} \mathbf{z}_j \mathbf{v}_j \quad (\text{B.3})$$

where \mathbf{z}_i is i th component of \mathbf{z} .

B.2.2. Variational auto-encoder (VAE)

Table B2 shows encoder-decoder models for VAE, whose network architecture is based on either MLP or CNN. In VAE, \mathbf{z} is given by the following sampling procedure: $\mathbf{z} = \boldsymbol{\mu} + \boldsymbol{\sigma} \odot \mathbf{z}_{\text{noise}}$ and $\mathbf{z}_{\text{noise}} \sim \mathcal{N}(\mathbf{0}, \mathbf{I})$, where $\boldsymbol{\mu}$ and $\boldsymbol{\sigma}$ are substantial outputs generated by a neural network, \odot is the element-wise product, and $\mathcal{N}(\mathbf{0}, \mathbf{I})$ is the normal distribution of mean $\mathbf{0}$ and covariance \mathbf{I} . Here, $\mathbf{0}$ is the zero vector and \mathbf{I} is the identity matrix of 10×10 .

Table B2. VAE network architectures.

(a) VAE				
Encoder				
Layer	Input Dim	Output Dim	Activation	
Linear	150	125	ReLU	
Linear	125	75	ReLU	
Linear	75	50	ReLU	
Linear	50	10×2	—	
Sampling	10×2	10	—	
Decoder				
Linear	10	50	ReLU	
Linear	50	75	ReLU	
Linear	75	125	ReLU	
Linear	125	150	-	
(b) Convolutional VAE				
Encoder				
Layer	Input Dim	Output Dim	Kernel	Activation
Conv1D	150×1	75×8	3×8	ReLU
Conv1D	75×8	38×16	3×16	ReLU
Conv1D	38×16	19×24	3×24	ReLU
Conv1D	19×24	10×32	3×32	ReLU
Flattening	10×32	320×1	—	—
Linear	320×1	10×2	—	—
Sampling	10×2	10×1	—	—
Decoder				
Linear	10×1	320×1	—	—
Reshaping	320×1	10×32	—	—
DeConv1D	10×32	19×24	3×24	ReLU
DeConv1D	19×24	38×16	3×16	ReLU
DeConv1D	38×16	75×8	3×8	ReLU
DeConv1D	75×8	150×8	3×8	ReLU
Conv1D	150×8	150×1	1×1	ReLU
Linear	150×1	150×1	—	

For VAE training, the following term is added to the loss function (23):

$$\text{KL}(\mathcal{N}(\boldsymbol{\mu}, \boldsymbol{\Sigma}) \| \mathcal{N}(\mathbf{0}, \mathbf{I})) = \frac{1}{2} \sum_{i=1}^{10} (\boldsymbol{\mu}_i^2 + \boldsymbol{\sigma}_i^2 - \log \boldsymbol{\sigma}_i - 1) \quad (\text{B.4})$$

where KL is Kullback-Leibler divergence and $\boldsymbol{\Sigma}$ is a 10×10 diagonal matrix whose (i, i) entry is $\boldsymbol{\sigma}_i$. This term enables VAE to learn dense and smooth latent space embedding in or near $\mathcal{N}(\mathbf{0}, \mathbf{I})$ [31, 50, 58].

B.2.3. β -Variational Auto-encoder (β -VAE)

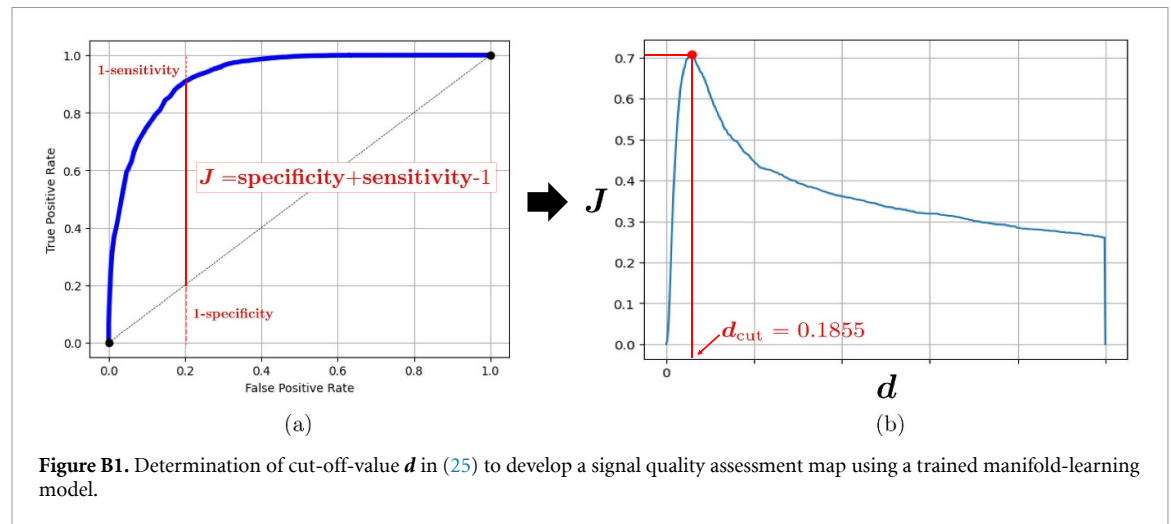
β -VAE differs with VAE in terms of loss function while sharing a model architecture. For some $\beta \in \mathbb{R}$, $\beta \times \text{KL}$ is added to the loss (23) instead of (B.4) (i.e. VAE is the case of $\beta = 1$). This simple weighting is known to be advantageous on disentangled representation learning of underlying factors [25]. We determined an optimal β as the empirical best. Table B3 showed SQI performance variation about β in the dataset where the scale and size normalization using linear interpolation were applied.

B.2.4. Determination of cut-off-value \mathbf{d}

Figures B1(a) and (b) show a case of selecting the cut-off-value \mathbf{d} in (25). Figure B1(a) shows a ROC curve obtained by varying \mathbf{d} from 0 to ∞ . Figure B1(b) shows computed values of \mathbf{J} with respect to values of \mathbf{d} . We selected a cut-point \mathbf{d}_{cut} such that maximizing \mathbf{J} . In our experiments, the \mathbf{d}_{cut} value was 0.3412 for PCA, 0.1855 for VAE, 0.1814 for β -VAE, 0.1830 for CVAE, and 0.1678 for β -CVAE in the case with scale and linear interpolation-based size normalization.

Table B3. β -VAE performance comparison about varying β .

		β -VAE					β -CVAE				
		$\beta = \frac{1}{3}$	$\beta = \frac{1}{2}$	$\beta = 1$	$\beta = 2$	$\beta = 3$	$\beta = \frac{1}{3}$	$\beta = \frac{1}{2}$	$\beta = 1$	$\beta = 2$	$\beta = 3$
Test	Accuracy	0.9060	0.9092	0.9066	0.8951	0.9221	0.9208	0.9298	0.9292	0.9195	0.9189
	PPV	0.9694	0.9680	0.9687	0.9682	0.9672	0.9750	0.9739	0.9688	0.9663	0.9663
	NPV	0.6151	0.6282	0.6181	0.5802	0.6900	0.6617	0.7011	0.7100	0.6720	0.6693
	Sensitivity	0.9203	0.9255	0.9218	0.9084	0.9441	0.9322	0.9441	0.9486	0.9397	0.9389
	Specificity	0.8142	0.8047	0.8095	0.8095	0.7952	0.8476	0.8380	0.8047	0.7904	0.7904
	AUC	0.9503	0.9439	0.9513	0.9426	0.9489	0.9531	0.9603	0.9528	0.9528	0.9471



B.3. Hyper-parameters

This subsection describes in detail hyper-parameters used for network training. For the sake of simplicity, we report the parameters for learning a SQI map with scale and size normalization using linear interpolation. For the discriminative models, the MLPs were trained for 500 epochs with a learning rate of 10^{-4} . By comparing validation results, we selected the models from the 480th and 440th epochs for MLP1 and MLP2, respectively. The VGG models were trained for 300 epochs with a learning rate of 10^{-4} . The models from the 280th, 280th, and 160th epochs were chosen for VGG16-3, VGG16-4, and VGG16-5, respectively. For the manifold learning models, VAE and β -VAE were trained for 10 000 epochs with a learning rate of 10^{-5} , while CVAE and β -CVAE were trained for 500 epochs with a learning rate of 10^{-4} . We chose the models from the 9000th, 8000th, 450th, and 400th epochs, respectively.

ORCID iDs

Chang Min Hyun <https://orcid.org/0000-0002-7072-7489>

Kyoungun Lee <https://orcid.org/0000-0002-8520-8999>

References

- [1] Adler A, Guardo R and Berthiaume Y 1996 Impedance imaging of lung ventilation: do we need to account for chest expansion? *IEEE Trans. Biomed. Eng.* **43** 414–20
- [2] Akobeng A K 2007 Understanding diagnostic tests 3: receiver operating characteristic curves *Acta Paediatr.* **96** 644–7
- [3] An J and Cho S 2015 Variational autoencoder based anomaly detection using reconstruction probability *Special Lecture on IE vol 2* pp 1–18
- [4] Adler A and Boyle A 2017 Electrical impedance tomography: tissue properties to image measures *IEEE Trans. Biomed. Eng.* **64** 2494–504
- [5] Askari A T and Messerli A W 2019 *Cardiovascular Hemodynamics* 2nd edn (Cham: Humana Press)
- [6] Alfaras M, Soriano M C and Ortin S 2019 A fast machine learning model for ECG-based heartbeat classification and arrhythmia detection *Front. Phys.* **7** 103
- [7] Brown B H, Leathard A, Sinton A, McArdle F J, Smith R W M and Barber D C 1992 Blood flow imaging using electrical impedance tomography *Clin. Phys. Physiol. Meas.* **13** 175–9
- [8] Boyle A and Adler A 2010 Electrode models under shape deformation in electrical impedance tomography *J. Phys.: Conf. Ser.* **224** 012051
- [9] Borges J B *et al* 2012 Regional lung perfusion estimated by electrical impedance tomography in a piglet model of lung collapse *J. Appl. Physiol.* **112** 225–36

- [10] Belo D, Rodrigues J, Vaz J R, Pezarat-Correia P and Gamboa H 2017 Biosignals learning and synthesis using deep neural networks *Biomedical Eng. Online* **16** 1–17
- [11] Buda M, Maki A and Mazurowski M A 2018 A systematic study of the class imbalance problem in convolutional neural networks *Neural Netw.* **106** 249–59
- [12] Cramer J S 2002 The origins of logistic regression *Tinbergen Inst. Working* **4** 1–15
- [13] Chapelle O, Scholkopf B and Zien A 2009 Semi-supervised learning (chapelle, o. et al, eds.; 2006)[book reviews] *IEEE Trans. Neural Netw.* **20** 542
- [14] Celin S and Vasanth K 2018 ECG signal classification using various machine learning techniques *J. Med. Syst.* **42** 1–11
- [15] Cao K, Wei C, Gaidon A, Arechiga N and Ma T 2019 Learning imbalanced datasets with label-distribution-aware margin loss *Advances in Neural Information Processing Systems vol 32* pp 1–12
- [16] Charlton P H, Bonnici T, Tarassenko L, Clifton D A, Beale R, Watkinson P J and Alastruey J 2021 An impedance pneumography signal quality index: design, assessment and application to respiratory rate monitoring *Biomed. Sig. Proc. Cont.* **65** 102339
- [17] Dai T, Gómez-Laberge C and Adler A 2008 Reconstruction of conductivity changes and electrode movements based on EIT temporal sequences *Physiol. Meas.* **29** S77–S88
- [18] Deibele J M, Luepschen H and Leonhardt S L 2008 Dynamic separation of pulmonary and cardiac changes in electrical impedance tomography *Physiol. Meas.* **29** S1–S14
- [19] Frerichs I, Becher T and Weiler N 2014 Electrical impedance tomography imaging of the cardiopulmonary system *Curr. Opin. Crit. Care* **20** 323–32
- [20] Goodfellow I, Bengio Y and Courville A 2016 *Deep Learning* (Cambridge, MA: MIT Press)
- [21] Hinton G E and Salakhutdinov R R 2006 Reducing the dimensionality of data with neural networks *Science* **313** 504–7
- [22] Hinton G E 2007 Learning multiple layers of representation *Trends Cogn. Sci.* **11** 428–34
- [23] He H and Garcia E A 2009 Learning from imbalanced data *IEEE Trans. Knowl. Data Eng.* **21** 1263–84
- [24] Hajian-Tilaki K 2013 Receiver operating characteristic (ROC) curve analysis for medical diagnostic test evaluation *Caspian J. Intern. Med.* **4** 627
- [25] Higgins I, Matthey L, Pal A, Burgess C, Glorot X, Botvinick M, Mohamed S and Lerchner A 2017 beta-vae: learning basic visual concepts with a constrained variational framework *Int. Conf. on Learning Representations (Palais des Congrès Neptune, Toulon, France, 24–26 April 2017)* pp 1–22
- [26] Hyun C M, Baek S H, Lee M, Lee S M and Seo J K 2021 Deep learning-based solvability of underdetermined inverse problems in medical imaging *Med. Image Anal.* **69** 101967
- [27] Jolliffe I T and Cadima J 2016 Principal component analysis: a review and recent developments *Phil. Trans. R. Soc. A* **374** 20150202
- [28] Jang G Y, Jeong Y J, Zhang T, Oh T I, Ko R-E, Chung C R, Suh G Y and Woo E J 2020 Noninvasive, simultaneous and continuous measurements of stroke volume and tidal volume using EIT: feasibility study of animal experiments *Sci. Rep.* **10** 11242
- [29] Kubicek W G, Patterson R P and Witsoe D A 1970 Impedance cardiography as a noninvasive method of monitoring cardiac function and other parameters of the cardiovascular system *Ann. New York Acad. Sci.* **170** 724–32
- [30] Kerrouche N, McLeod C N and Lionheart W R B 2001 Time series of EIT chest images using singular value decomposition and fourier transform *Physiol. Meas.* **22** 147–57
- [31] Kingma D P and Welling M 2013 Auto-encoding variational bayes (arXiv:1312.6114)
- [32] Kingma D P and Ba J 2014 Adam: A method for stochastic optimization (arXiv:1412.6980)
- [33] Lionheart W R B 1998 Boundary shape and electrical impedance tomography *Inverse Problems* **14** 139–47
- [34] Leonhardt S and Lachmann B 2012 Electrical impedance tomography: the holy grail of ventilation and perfusion monitoring *Intensive Care Med.* **38** 1917–29
- [35] Lopez-Raton M, Rodriguez-Alvarez M X, Cadarso-Suarez C and Gude-Sampedro F 2014 OptimalCutpoints: an R package for selecting optimal cutpoints in diagnostic tests *J. Stat. Softw.* **61** 1–36
- [36] LeCun Y, Bengio Y and Hinton G 2015 Deep learning *Nature* **521** 436–44
- [37] Luo W, Li Y, Urtasun R and Zemel R, 2017 Understanding the effective receptive field in deep convolutional neural networks (arXiv:170.04128)
- [38] Lee K, Woo E J and Seo J K 2017 A fidelity-embedded regularization method for robust electrical impedance tomography *IEEE Trans. Med. Imaging* **37** 1970–7
- [39] Lee J H, Park Y R, Kweon S, Kim S, Ji W and Choi C M 2018 A cardiopulmonary monitoring system for patient transport within hospitals using mobile internet of things technology: observational validation study *JMIR mHealth and uHealth* **6** e12048
- [40] Lee M H, Jang G Y, Kim Y E, Yoo P J, Wi H, Oh T I and Woo E J 2018 Portable multi-parameter electrical impedance tomography for sleep apnea and hypoventilation monitoring: feasibility study *Physiol. Meas.* **39** 124004
- [41] Lee K, Jang G Y, Kim Y and Woo E J 2021 Multi-channel trans-impedance leadforming for cardiopulmonary monitoring: algorithm development and feasibility assessment using *in vivo* animal data *IEEE Trans. Biomed. Eng.* **69** 1964–74
- [42] Pikkemaat R, Lundin S, Stenqvist O, Hilgers R-D and Leonhardt S 2014 Recent advances in and limitations of cardiac output monitoring by means of electrical impedance tomography *Anesth. Analg.* **119** 76–83
- [43] Putensen C, Hentze B, Muenster S and Muders T 2019 Electrical impedance tomography for cardiopulmonary monitoring *J. Clin. Med.* **8** 1176
- [44] Ravenswaaij-Arts C M A, Kollee L A A, Hopman J C W, Stoeltinga G B A and van Geijn H P 1993 Heart rate variability *Ann. Intern. Med.* **118** 436–47
- [45] Ruopp M D, Perkins N J, Whitcomb B W and Schisterman E F 2008 Youden Index and optimal cut-point estimated from observations affected by a lower limit of detection *Biom. J.* **50** 419–30
- [46] Soleimani M, Gómez-Laberge C and Adler A 2006 Imaging of conductivity changes and electrode movement in EIT *Physiol. Meas.* **27** S103–13
- [47] Seo J K and Woo E J 2013 *Nonlinear Inverse Problems in Imaging* (Chichester: Wiley)
- [48] Simonyan K and Zisserman A 2014 Very deep convolutional networks for large-scale image recognition (arXiv:1409.1556)
- [49] Schlegl T, Seebock P, Waldstein S M, Schmidt-Erfurth U and Langs G 2017 Unsupervised anomaly detection with generative adversarial networks to guide marker discovery *Int. Conference on Information Processing in Medical Imaging* (Cham: Springer) pp 146–57
- [50] Seo J K, Kim K C, Jargal A, Lee K and Harrach B 2019 A learning-based method for solving ill-posed nonlinear inverse problems: a simulation study of lung EIT *SIAM J. Imaging Sci.* **12** 1275–95
- [51] Sahoo S, Dash M, Behera S and Sabut S 2020 Machine learning approach to detect cardiac arrhythmias in ECG signals: a survey *IRBM* **41** 185–94

- [52] Van Horn G and Perona P 2017 The devil is in the tails: fine-grained classification in the wild (arXiv:1709.01450)
- [53] Van Engelen J E and Hoos H H 2020 A survey on semi-supervised learning *Mach. Learn.* **109** 373–440
- [54] Westterhof N *et al* 2019 *Snapshots of Hemodynamics* 3rd edn (Cham: Springer)
- [55] Wasimuddin M, Elleithy K, Abuzneid A-S, Faezipour M and Abuzagheh O 2020 Stages-based ECG signal analysis from traditional signal processing to machine learning approaches: a survey *IEEE Access* **8** 177782–803
- [56] Xu Y, Xiao T, Zhang J, Yang K and Zhang Z 2014 Scale-invariant convolutional neural networks (arXiv:1411.6369)
- [57] Yang L, Qu S, Zhang Y, Zhang G, Wang H, Yang B, Xu C, Dai M and Cao X 2022 Removing clinical motion artifacts during ventilation monitoring with electrical impedance tomography: introduction of methodology and validation with simulation and patient data *Front. Med.* (<https://doi.org/10.3389/fmed.2022.817590>)
- [58] Yun H S, Hyun C M, Baek S H, Lee S-H and Seo J K 2022 A semi-supervised learning approach for automated 3D cephalometric landmark identification using computed tomography *PLoS One* **17** e0275114
- [59] Zhang J and Patterson R P 2005 EIT images of ventilation: what contributes to the resistivity changes? *Physiol. Meas.* **26** S81–S92
- [60] Zlochiver S, Freemark D, Arad M, Adunsky A and Abboud S 2006 Parametric EIT for monitoring cardiac stroke volume *Physiol. Meas.* **27** S139–46
- [61] Zhu X and Goldberg A B 2009 *Introduction to Semi-Supervised Learning* (*Synthesis Lectures on Artificial Intelligence and Machine Learning* vol 3) (Springer) pp 1–130